Monthly Notices of the ROYAL ASTRONOMICAL SOCIETY

MNRAS **517,** 3459–3468 (2022) https://doi.org/10.1093/mnras/stac2858
Advance Access publication 2022 October 6

Stellar angular momentum can be controlled from cosmological initial conditions

Corentin Cadiou [1,3]★ Andrew Pontzen[1] and Hiranya V. Peiris[1,2]

[1]*Department of Physics and Astronomy, University College London, Gower Street, London WC1E 6BT, UK*
[2]*The Oskar Klein Centre for Cosmoparticle Physics, Department of Physics, Stockholm University, AlbaNova, SE-106 91 Stockholm, Sweden*
[3]*Lund Observatory, Department of Astronomy and Theoretical Physics, Lund University, Box 43, SE-221 00 Lund, Sweden*

Accepted 2022 October 3. Received 2022 September 16; in original form 2022 June 23

ABSTRACT

The angular momentum of galaxies controls the kinematics of their stars, which in turn drives observable quantities such as the apparent radius, the bulge fraction, and the alignment with other nearby structures. To show how angular momentum of galaxies is determined, we build high (35 pc) resolution numerical experiments in which we increase or decrease the angular momentum of the Lagrangian patches in the early universe. We perform cosmological zoom-in simulations of three galaxies over their histories from $z = 200$ to $z = 2$, each with five different choices for the angular momentum (15 simulations in total). Our results show that altering early universe angular momentum changes the timing and orbital parameters of mergers, which in turn changes the total stellar angular momentum within a galaxy's virial radius in a predictable manner. Of our three galaxies, one has no large satellite at $z = 2$; in this case, the specific angular momentum is concentrated in the central galaxy. Our changes to the initial conditions result in its stellar angular momentum changing over 0.7 dex (from 61 to 320 kpc km s^{-1}) at $z = 2$. This causes its effective radius to grow by 40 per cent, its v/σ parameter to grow by a factor of 2.6, and its bulge fraction to decrease from 0.72 to 0.57. This proof of concept illustrates how causal studies can contribute to a better understanding of the origin of galaxy scaling relations and intrinsic alignments.

Key words: methods: numerical – galaxies: formation – galaxies: haloes – dark matter.

1 INTRODUCTION

Angular momentum plays a major role in galaxy formation. In spiral galaxies, it dictates the size and alignment of the disc; elliptical galaxies, by contrast, are dispersion-supported and have on average eight times lower stellar specific angular momentum $j_\star$ at a given stellar mass (Fall 1983; Romanowsky & Fall 2012; Harrison et al. 2017; Fall & Romanowsky 2018; Espejo Salcedo et al. 2022). Moreover, the angular momentum of neighbouring galaxies is partially correlated. This effect, known as intrinsic alignment (Troxel & Ishak 2015), needs to be properly modelled to disentangle it from cosmic shear and thus ensure the success of upcoming cosmological weak-lensing surveys (*Euclid*, Laureijs et al. 2011; Vera Rubin Observatory, Ivezić et al. 2019).

Early explanations for the origin of galactic angular momentum assumed that the gas and dark matter (DM) within a given halo acquire identical spin, driven by tidal torques from the large-scale environment (Peebles 1969; Doroshkevich 1970; White 1984). Even though gas radiatively cools to form stars, in doing so it may conserve its angular momentum, so that stars in a galaxy would inherit the DM halo's spin (Fall & Efstathiou 1980; Mo, Mao & White 1998). Recent work shows that, at the population level, the specific angular momentum distributions of simulated galaxies and DM haloes are indeed strikingly similar (Danovich et al. 2015). On a per-object basis, their magnitudes are poorly correlated (Jiang et al. 2019); however, if one divides the population into bins in stellar mass, haloes with largest spin are revealed to host galaxies rotating about three times faster than those hosted in haloes with the smallest spin (Rodriguez-Gomez et al. 2022). This relationship is of high statistical significance, but is comparable in magnitude to the scatter in the population. Therefore, using the DM halo spin as a proxy for galactic angular momentum, as in some semi-analytical prescriptions (e.g. Somerville et al. 2008; Guo et al. 2011; Benson 2012), is noisy and may lead to mischaracterizations of the link between galaxy properties and large-scale structures. The spin directions also show significant misalignments, with the extent of the mismatch depending on redshift, mass, or the central/satellite nature of the host (Tenneti et al. 2014; Velliscig et al. 2015; Chisari et al. 2017).

Multiple explanations have been put forward to explain how the galaxy spin may decouple from the host halo spin. First, gas can cool even outside the halo and therefore the DM and baryons accreted into a halo do not necessarily originate in the precise same patch of the early universe (Kimm et al. 2011; Pichon et al. 2011; Liao et al. 2017). This in turn implies that the tidal torques differ between the two components. At high redshift, and for sufficiently low-mass galaxies, most of the gas and angular momentum flows into galaxies through cold flows (Dekel & Birnboim 2006; Tillson et al. 2015;

★ E-mail: corentin.cadiou@astro.lu.se

© 2022 The Author(s).
Published by Oxford University Press on behalf of Royal Astronomical Society. This is an Open Access article distributed under the terms of the Creative Commons Attribution License (https://creativecommons.org/licenses/by/4.0/), which permits unrestricted reuse, distribution, and reproduction in any medium, provided the original work is properly cited.

Downloaded from https://academic.oup.com/mnras/article/517/3/3459/6750247 by Deutsches Elektronen Synchrotron user on 08 December 2022

Stewart et al. 2017), allowing the gas to acquire a larger angular momentum than DM prior to accretion (Stewart et al. 2011; Danovich et al. 2015; Cadiou, Dubois & Pichon 2022). It was also recently suggested that DM collapses faster than gas, causing the inner parts of the halo to 'spin up' the gas through torques (Li et al. 2022).

A second source of galactic angular momentum is from mergers. The orbital angular momentum from mergers causes the magnitude and orientation of the DM halo spin to change near-instantaneously (Vitvitska et al. 2002; Benson, Behrens & Lu 2020), but the effects on the galaxy are slower and more complex. The orientation and magnitude of spin in the post-merger disc eventually depend on the fraction of orbital angular momentum conserved during the merger, and on the efficiency and angular momentum richness of the post-merger star formation that rebuilds the disc. Consequently, the final result of a galaxy merger can depend on the gas fraction and morphology of the progenitors (Barnes & Hernquist 1996; Naab & Burkert 2003; Lotz et al. 2008; Governato et al. 2009; Athanassoula et al. 2016; Garrison-Kimmel et al. 2018; Lagos et al. 2018), the orbital configuration of the merging system (Martin et al. 2018; Jackson et al. 2020; Zeng, Wang & Gao 2021), and feedback and cooling processes at play (Cox et al. 2006; Robertson et al. 2006).

Even once gas is inside a halo, a variety of processes determine whether it is incorporated into the disc, and therefore how it changes the stellar angular momentum. Cold flows may be hydrodynamically disrupted (see e.g. Mandelker et al. 2016, 2019, 2020; Cornuault et al. 2018; Padnos et al. 2018; Aung et al. 2019) or be blown away by feedback (Dubois et al. 2013; Ramsøy et al. 2021). Centrally concentrated supernova feedback may preferentially expel low-angular-momentum gas from the centre of galaxies, resulting in an amplification of the spin of the galactic disc (Brook et al. 2011; Übler et al. 2014; Genel et al. 2015). Finally, accretion of counter-rotating material may lead to a rapid contraction of a galactic disc (Dekel & Burkert 2014; Zolotov et al. 2015), generating a starburst and associated feedback energy that can expel remaining gas.

In summary, the final angular momentum of galaxies depends on (a) the angular momentum originating in the cosmological initial conditions, (b) how this angular momentum is transported from cosmological to galactic scales via smooth accretion and mergers, and (c) what fraction of this angular momentum remains in the galaxy and its disc. These dependences are complex, raising the question of whether or not galaxies retain a clear memory of angular momentum generated by tidal torques, and whether the different evolution of the DM and galactic spins results in their (partial) decorrelation. Beyond its inherent interest in galaxy formation theory, answering that question is ultimately essential for understanding the amplitude of intrinsic alignments for weak lensing.

In this paper, we test whether galaxies retain a memory of their cosmologically acquired angular momentum and whether the magnitudes of the angular momenta of the stars and the DM are linked through this memory. We perform a numerical experiment in which we resimulate three galaxies five times each, systematically modifying the angular momentum acquired by the baryons in the linear early universe. This is accomplished by creating four 'genetically modified' versions of the initial conditions, using the technique of Roth, Pontzen & Peiris (2016) to ensure the changes are minimal and consistent with the cosmological statistics. The approach was recently extended to the case of angular momentum by Cadiou, Pontzen & Peiris (2021). After resimulating the additional initial conditions, we measure the stellar angular momentum in the galaxy at $z \approx 2$, and assess the degree to which it correlates with the angular momentum in the initial conditions. We employ cosmological zoom-in simulations with state-of-the-art physics using the code RAMSES (Teyssier 2002).

By performing this experiment in a zoom cosmological simulation, we capture angular momentum acquisition at cosmological scale, its transport into galaxies, and the relevant physical processes in play at galactic scale. This approach allows us to study the formation of a *specific* galaxy, with the mass assembly and cosmological environment varying only minimally between simulations. As such, any confounding factors are strongly suppressed. This gives a complementary view of the acquisition of angular momentum, allowing us to begin investigating the causal mechanisms that establish statistical correlations in the broader population. The goal is to build towards better models of galaxy and halo angular momentum acquisition, which will ultimately shed light on galaxy scaling relations and intrinsic alignments.

The structure of the paper is as follows. In Section 2, we describe our numerical set-up and how we genetically modify the initial conditions to alter the angular momentum of three simulated galaxies. We then present our results in Section 3, before discussing their implications in Section 4.

2 METHOD

2.1 Simulations

All our simulations are performed within a cosmology that has a total matter density of $\Omega_{\rm m} = 0.3089$, a dark energy density of $\Omega_\Lambda = 0.6911$, a baryonic mass density of $\Omega_{\rm b} = 0.0486$, a Hubble constant of $H_0 = 67.74\,{\rm km\,s^{-1}\,Mpc^{-1}}$, a linear variance at 8 Mpc of $\sigma_8 = 0.8159$, and a power spectrum index of $n_{\rm s} = 0.9667$, compatible with a *Planck* 2015 cosmology (Planck Collaboration XXIII 2015).

We first generate a 512^3 DM-only simulation of a cosmological box of comoving side length $100\,h^{-1}$ Mpc, using initial conditions generated by GENETIC (Stopyra et al. 2021), which enables the construction of accurate genetic modifications. From this, we select three haloes of virial mass $M_{\rm vir} \approx 10^{12}\,{\rm M}_\odot$ at $z = 2$ for resimulation at high resolution. Galaxies of this mass range and this redshift display a diverse range of morphologies (see e.g. Tamburri et al. 2014), which allows us to study the onset of the Hubble sequence. We select three haloes, hereafter haloes A, B, and C, with no major merger since $z = 2.5$ and no massive nearby neighbour within 500 kpc in the low-resolution DM-only simulation. Here and in the following, we define major mergers as mergers with DM halo mass ratios larger than 1:8. The haloes are chosen 'blind', i.e. randomly from haloes of the appropriate mass range matching the merger and neighbour criteria. When increasing the resolution, mergers below the resolution limit of the low-resolution simulations may appear, as we discuss below. In each of the three cases, we identify the Lagrangian patch of particles extending out to three virial radii, and populate the corresponding regions of the initial conditions with high-resolution DM particles.

We perform these three simulations with hydrodynamics using the adaptive mesh refinement (AMR) code RAMSES (Teyssier 2002), adopting a minimum cell size of 35 pc, and a mass resolution of $M_{\rm DM} = 1.6 \times 10^6\,{\rm M}_\odot$ and $M_\star = 1.1 \times 10^4\,{\rm M}_\odot$ for DM and stars, respectively. We use the cell resolution as the gravitational softening length for gas and stellar particles and the maximum resolution attained in the DM-only run (constant 566 pc comoving, i.e. 186 pc at $z = 2$) for DM particles (same mass resolution and softening lengths as NewHorizon, Dubois et al. 2021 and Obelisk, Trebitsch et al. 2021). We employ Monte Carlo tracer particles to recover the Lagrangian history of the baryons, as described in Cadiou, Dubois & Pichon (2019). Lagrangian particles are passive tracers

Downloaded from https://academic.oup.com/mnras/article/517/3/3459/6750247 by Deutsches Elektronen Synchrotron user on 08 December 2022

that follow mass flows between cells of the AMR grid. Monte Carlo tracer particles achieve this by moving tracers from one cell to another with a probability proportional to the mass flux between the cells. Similarly, star formation, black hole accretion, and feedback processes are traced following fluxes between gas cells, stellar particles, and supermassive black hole particles.

We use sub-grid baryonic physics following the approach of NewHorizon (Dubois et al. 2021) with the same resolution. These models have been shown to reproduce the formation of massive discs (Park et al. 2019, 2021) and to recover the observed size evolution of galaxies (Dubois et al. 2021). In brief, star formation is allowed above a gas density of $n_0 = 10\,\mathrm{cm}^{-3}$ with a Schmidt law; the stellar population is sampled with a Kroupa (2001) initial mass function; and the mass-loss fraction from supernova explosions is $\eta_{\rm SN} = 32$ per cent with a metal yield (mass ratio of the newly formed metals over the total ejecta) of 0.05. Type II supernovae are modelled with the mechanical feedback model of Kimm et al. (2015) with a boost in momentum due to early ultraviolet (UV) pre-heating of the gas following (Geen et al. 2015). The simulations also track the formation of supermassive black holes and their energy release through active galactic nucleus (AGN) feedback. Further details about the simulations can be found in Appendix A.

We extract galaxy and halo catalogues using ADAPTAHOP (Aubert, Pichon & Colombi 2004), using the 'Most massive Sub-node Method' and the parameters proposed in Tweed et al. (2009). The density is computed from the 20 nearest neighbours and we use a linking length parameter of $b = 0.2$. For each galaxy, we compute the half-mass radius $R_{1/2}$, defined as the radius that contains half the total stellar mass, $M_\star(< R_{1/2}) = M_\star(< R_{\rm vir})/2$. We then perform a kinematic decomposition to compute the bulge-to-total mass ratio, B/T. To that end, we first compute the stellar angular momentum and project all particles in cylindrical coordinates, where the z-axis is parallel to the angular momentum vector. We include the mass of particles in the kinematic bulge if the magnitude of their tangential velocity satisfies $v_\theta^2 < v_r^2 + v_z^2$. Finally, we also compute the velocity dispersion parameter, $v/\sigma \equiv \langle v_\theta \rangle / \sqrt{\langle v^2 \rangle}$, where the average is a mass-weighted sum over all stellar particles.

2.2 Angular momentum modifications

With three galaxy simulations in hand, we next resimulate each with a variety of different angular momenta. We apply the genetic modification approach (Roth et al. 2016), extended for the case of angular momentum as described by Cadiou et al. (2021). As per Roth et al. (2016), the appropriate region in the early universe is systematically modified while maintaining consistency with the Gaussianity and power spectrum specified by cosmology. The changes made to the field are minimal so that other structures and large-scale filaments are nearly unaffected by the modifications to any given galaxy. Modifications are applied to the linear initial conditions, in which tidal fields and velocity fields are both derived from a single gravitational potential. For this reason, changing the angular momentum of a patch also scales the magnitude of the gravitational torques acting on the patch, consistent with expectations from tidal torque theory: the initial angular momentum is always small, and the torques are responsible for it growing over time. For example, an elongated region of the initial conditions can be 'spun up' by adding a small overdensity on its leading edge and corresponding underdensity on the trailing side. For a formal derivation and presentation of the method, see Cadiou et al. (2021).

To enable the modification, first a suitable patch of the early universe must be identified in which the angular momentum will be changed. The reference galaxies have a DM spin parameter (Bullock et al. 2001) $\lambda \equiv j/\sqrt{2} V_{\rm vir} R_{\rm vir} = 0.05$, 0.11, and 0.10, respectively. We note that though the haloes are selected in the low-resolution DM-only simulation to have no major mergers between $z = 2.5$ and 2, they do have mergers in the high-resolution simulations with mass ratio 1:5 at $z = 2.3$ for halo A, mass ratio 1:5 at $z = 2.2$ for halo B, and mass ratio 1:6 at $z = 2.3$ for halo C. For each halo, we locate the central galaxy at $z = 2$ in the reference zoom-in hydrodynamical simulation. We then select all tracer particles (gas, stars, and those accreted in supermassive black holes; see Cadiou et al. 2019 for details) within the galaxy, defined by the region within $4R_{1/2}$ at $z = 2$. We trace back the baryons to the initial conditions to find the baryonic Lagrangian patch of the galaxies.[1] This baryonic Lagrangian patch is different from the DM patch one obtains when tracing back the DM particles instead (Liao et al. 2017).

We scale the magnitude of the initial angular momentum with the genetic modification technique described above, applied to the baryonic patch at $z = 200$. We note that, due to correlations in the initial conditions, changes to the baryonic initial angular momentum may also affect the DM angular momentum. For each of the three reference galaxies, we generate four additional galaxy initial conditions where the angular momentum j_0 of the baryonic patch has been scaled relative to the reference angular momentum $j_{0,\,\rm ref}$ by a factor $j_0/j_{0,\,\rm ref} = 0.66$, 0.8, 1.2, and 1.5, respectively. Such amplitudes are large enough to sample a wide range of stellar angular momentum, as we will show later, while still allowing control of the angular momentum of individual regions in the evolved universe within a few tens of per cent (Cadiou et al. 2021). We keep the mean density of the entire DM halo Lagrangian patch fixed, which causes the halo mass to be almost unchanged at $z = 2$ (to an extent that we will shortly quantify).

We use these genetically modified initial conditions to perform 12 additional hydrodynamical zoom-in simulations. In total, we thus have a sample of 3 galaxies with 5 different angular momentum scenarios each, for a total of 15 simulations. However, we subsequently removed from the sample the special case of halo C × 1.5 because the interpretation is hindered by a large delay in its assembly; this is discussed further in Section 3.

At the end of the simulation, the host haloes in the remaining 14 simulations have masses of $M_{\rm DM} \approx 10^{12}\,\mathrm{M}_\odot$ and stellar mass within the virial radius of $M_\star(< R_{\rm vir}) \approx 10^{11}\,\mathrm{M}_\odot$. We report in the left-hand column of Table 1 the halo masses for the three reference simulations, as well as their minimum and maximum value in the 11 modified simulations, showing that the values change from the reference value by 7 per cent at most once the single case of C × 1.5 has been excluded. The middle column shows the stellar mass interior to the virial radius, which likewise is very stable, varying from the reference value by at most 10 per cent. The right-hand column shows the stellar mass in the central galaxy, which is more variable (up to almost a factor of 2). This is because the modification to the angular momentum changes the orbital trajectory of the satellites even after they have entered the virial radius, which in turn means they merge with the central galaxy at differing times relative to the end of the simulation.

[1] There are on average eight tracers per cell in the initial conditions, and we consider any cell where more than five tracer particles end in the galaxy to belong to the patch.

Downloaded from https://academic.oup.com/mnras/article/517/3/3459/6750247 by Deutsches Elektronen Synchrotron user on 08 December 2022

Table 1. Minimum, maximum, and reference values of the DM halo mass, the stellar mass within the virial radius, and the stellar mass in the central galaxy at the end of the simulations at $z = 1.95$. Modifying the angular momentum keeps the halo mass and the stellar mass in the virial radius fixed within a few tens of per cent. The mass of the central galaxy changes due to changes in the orbital trajectory of satellites, which advance or delay their merger.

Halo		$M_{\rm DM}$ ($\times 10^{11}\,{\rm M}_\odot$)	$M_\star(<R_{\rm vir})$ ($\times 10^{10}\,{\rm M}_\odot$)	$M_{\rm gal,\star}$ ($\times 10^{10}\,{\rm M}_\odot$)
A	Minimum	9.8	9.8	6.3
	Reference	10.4	10.9	9.9
	Maximum	10.4	11.2	10.4
B	Minimum	10.2	10.6	4.5
	Reference	10.6	10.8	8.7
	Maximum	10.6	11.4	8.7
C	Minimum	10.0	09.9	6.6
	Reference	10.8	11.2	7.3
	Maximum	10.9	11.2	8.5

3 RESULTS

Our goal is to quantify how changes in the initial angular momentum of the baryonic Lagrangian patch affect the angular momentum and observable galaxy properties at redshift $z = 2$. For each of our simulations, we first measure the specific angular momentum of all the baryons, of all the stars, and of all the DM within the virial radius at $z = 2$, $\boldsymbol{j}_{\rm b}$, $\boldsymbol{j}_\star$, and $\boldsymbol{j}_{\rm DM}$, including particles in satellite galaxies. We define the centre of the galaxy using a shrinking-sphere approach on the stellar density (Power et al. 2003)[2] and we then compute the angular momentum around this centre. In order to quantify how well we can control these angular momenta, from each modified simulation, we calculate $j(z = 2)/j_{\rm ref}(z = 2)$ separately for stars, baryons, and DM. Fig. 1 compares this measured ratio to the imposed ratio in the initial conditions at $z = 200$. In all but one case (halo B $\times$ 0.66), the change of stellar angular momentum at $z = 2$ is in the direction expected (left-hand panel): its value increases (resp. decreases) when we increase (resp. decrease) the initial angular momentum. For the one contrary case (halo B $\times$ 0.66), we were unable to identify a single cause of the unexpectedly large angular momentum at $z = 2$, but we note that this system has a complex merger history that may introduce non-linear interactions between the orbits of different sub-haloes. We discuss this point further below.

For halo A $\times$ 1.5, the final angular momentum is increased but by a surprisingly large factor of 4. In this case, the central galaxy is not relaxed and is undergoing a 1:2 merger event. At $z = 2.0$, the companion is at its apocentre after reaching pericentre at $z = 2.06$. This causes the centre of the central galaxy about which angular momentum is computed to be significantly offset from the centre of mass of the system. Overall, based on this initial set of simulations, the relation between initial conditions and final stellar angular momentum is strong; the Spearman correlation coefficient between the initial modification and the measured change is 83 per cent.

Our control of the angular momentum is somewhat weaker for baryons and DM, for which we measure a statistical correlation of $\approx$70 per cent (see Fig. 1, central and right-hand panels). We have previously shown that particles in the outskirts of haloes dominate the halo spin; therefore, small changes to the halo finder's boundary can cause apparently chaotic changes in the angular momentum of DM and gas (Cadiou et al. 2021). Stars, by contrast, typically occupy the deepest parts of the potential and their angular momentum is therefore less impacted by changes in the halo's boundary.

While the total angular momentum of stars inside the halo can be controlled, this quantity includes the contribution from satellites. We now focus on a case where there are no major satellites, in order to investigate the case where we control the angular momentum of the central galaxy itself. We count 'major' satellites as having a stellar mass ratio more significant than 1:8; by this definition, galaxy A has no major satellite inside its virial radius at $z = 2$. This remains true in three of the four modifications (with $\times$0.66, $\times$0.8, and $\times$1.2 angular momentum); in the case of $\times$1.5, a 1:2 galaxy merger is delayed until after $z = 2$ due to its increased orbital angular momentum. In the cases where all major galaxy mergers have completed, the stellar mass and angular momentum within the virial radius are dominated by the central galaxy's disc. We show in Fig. 2 mock images in rest-frame u, v, i Sloan Digital Sky Survey (SDSS) bands for the red, green, and blue channels, respectively, together with the galaxy's stellar specific angular momentum, stellar mass, stellar half-mass radius, bulge-to-total mass fraction, and v/σ parameter. As we increase angular momentum in the initial conditions, the value of the galaxy's stellar angular momentum at $z = 2$ increases while its stellar mass remains relatively constant. This allows us to explore how the galaxy's angular momentum is reflected in its observable properties.

Qualitatively, the galaxy displays a ring-like structure in the lowest angular momentum simulation (left) that progressively disappears as angular momentum increases. To understand its origin, we measure the angle $\cos\theta = \hat{\boldsymbol{j}}_\star \cdot \hat{\boldsymbol{j}}_{\rm orbit}$ between the direction of the central galaxy's angular momentum, $\hat{\boldsymbol{j}}_\star$, and the orbital angular momentum of the last major merger, $\hat{\boldsymbol{j}}_{\rm orbit} = \boldsymbol{r} \times \boldsymbol{v}/|\boldsymbol{r} \times \boldsymbol{v}|$. Here, $\boldsymbol{r}$ and $\boldsymbol{v}$ are the position and bulk velocity of the satellite relative to the central galaxy. We average the angle along the satellite during its infall through the virial radius. An angle of 0° corresponds to an orbit in the plane of the galaxy's disc, while an angle of 90° corresponds to an orbit perpendicular to it. We find that, as we modify angular momentum upwards, the orbit becomes increasingly coplanar: the mean angle during the infall through the virial radius (from 60 to 20 kpc) is 77°, 71°, 63°, and 58° for the $\times$0.66, $\times$0.8, reference, and $\times$1.2 cases, respectively. The mean angle measured just before the merger (at a separation less than 20 kpc) is 52°, 50°, 31°, and 27°. We verified that the ring is made of stars formed since the last major merger and is still star-forming at the end of the simulation, and that the ring is coplanar with the orbit of the last major merger.

We thus interpret the ring visible in Fig. 2 (left-hand panel) as being induced by the last major merger that falls through the virial radius almost perpendicular (77°) to the already-existing disc before realigning itself partially (52°). Conversely, in the increased angular momentum case (right-hand panel), the orbit of the satellite upon passing through the virial radius is already more aligned with the galaxy's spin (58°) and becomes almost coplanar by the time it merges (27°). As a consequence, modifications lead to a factor of 6 increase in stellar angular momentum from the lowest angular momentum scenario to the highest angular momentum one, while maintaining a fixed stellar mass. From lowest to highest angular momentum simulations, the half-mass radius $R_{1/2}$ increases by 40 per cent from 0.9 to 1.3 kpc. Similarly, the galaxy's bulge-to-total mass fraction decreases by 25 per cent, while the post-merger v/σ parameter increases by $\times$2.6. While previous statistical studies have suggested that morphology can be changed by the alignment of a merger (Hopkins et al. 2009; Martin et al. 2018; Jackson et al.

[2]We find the barycentre within a sphere of radius $R_{\rm vir}$. We then recentre the sphere about this point, shrink it by 30 per cent, and repeat the first step. The procedure stops when there are fewer than 100 particles in the selected region.

Downloaded from https://academic.oup.com/mnras/article/517/3/3459/6750247 by Deutsches Elektronen Synchrotron user on 08 December 2022

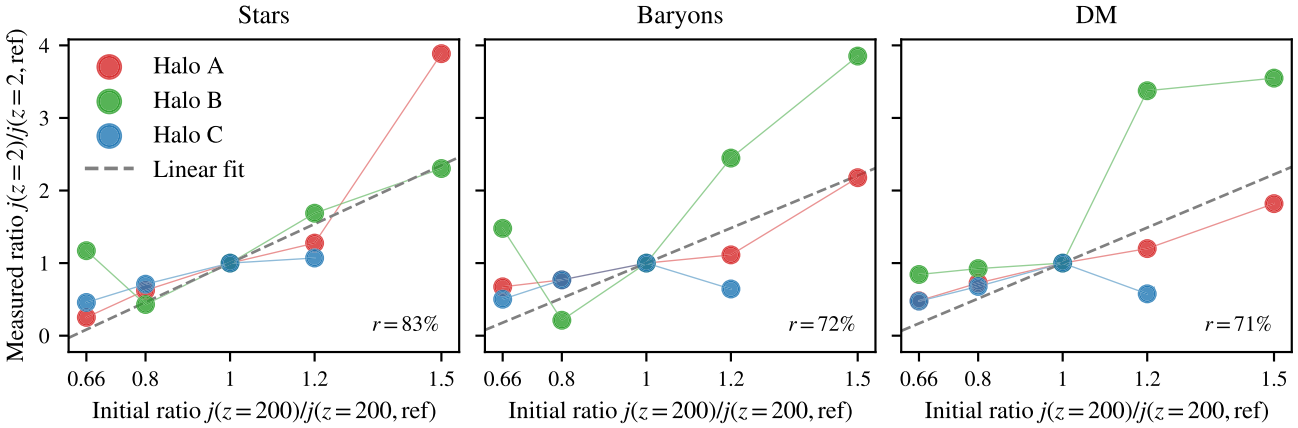

Figure 1. We measure the stellar (left-hand panel), baryonic (central panel), and DM (right-hand panel) specific angular momentum within $R_{\rm vir}$ at $z = 2$ and compare it to the initial angular momentum change of the baryonic Lagrangian patch at $z = 200$. The Pearson correlation coefficient between the two quantities is reported in each panel. We can control the final stellar angular momentum within $R_{\rm vir}$ through modifications in the initial conditions; the baryons and DM angular momentum also respond in a correlated way. In the case of galaxies A × 1.5 and B × 0.66, the stellar angular momentum does not change linearly. Galaxy A × 1.5 is undergoing a 1:2 merger, with the companion reaching its first apocentre at $z = 2$. Galaxy B × 0.66 has a complex series of mergers, as described in the text.

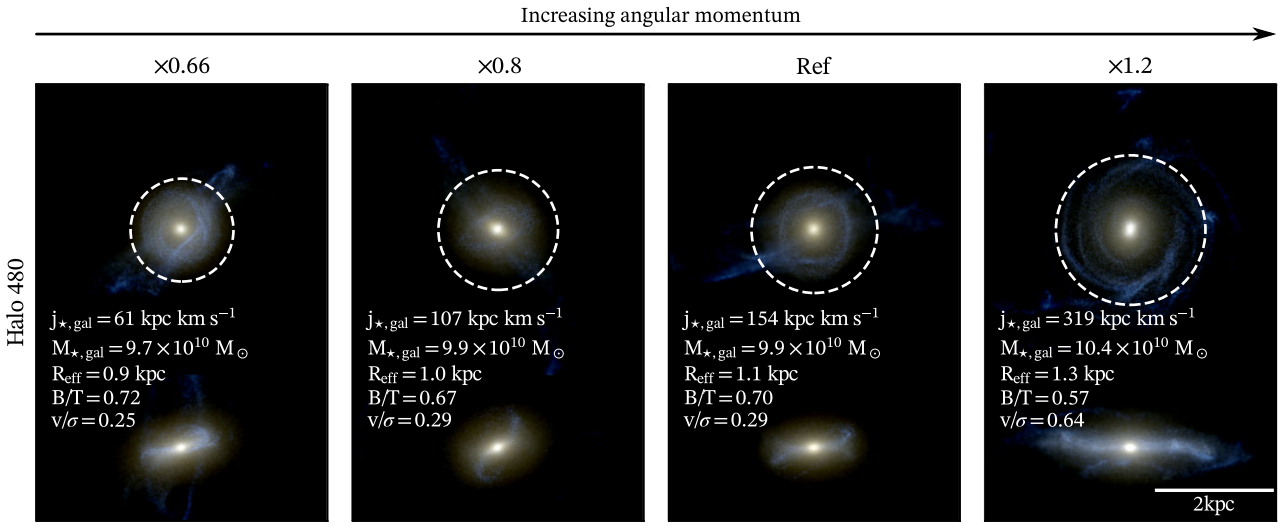

Figure 2. Mock images of the galaxy in halo A at $z = 1.95$ sorted by increasing stellar angular momentum (from left to right). We show here the stellar specific angular momentum, mass, effective radius, and bulge-to-total mass fraction measured *in the galaxy*. The top row shows face-on mock images and the bottom row shows edge-on images. At fixed mass, galaxies with higher angular momentum have a more pronounced stellar disc, are more spatially extended, and have a smaller bulge and a higher velocity-to-velocity dispersion v/σ parameter. Conversely, galaxies with decreased stellar angular momentum are less discy, more compact, and bulgy.

2020; Zeng et al. 2021), our study provides the first direct test of this on individual galaxies in a cosmological environment.

The importance of satellites in delivering angular momentum, and the effect that angular momentum has on the orbital dynamics, can also be seen in Fig. 3, where we plot the stellar angular momentum within the virial radius, $j_\star(r < R_{\rm vir})$, as a function of time. Halo A, the galaxy that we have just considered in detail, is shown in the upper panel. The large jumps in angular momentum correspond to the moment when massive satellite galaxies fall through the virial radius; we show infall times with arrows for all mergers with a stellar mass ratio larger than 1:8. (Note that the galaxy mergers happen a few dynamical times later than the infall time, depending on the trajectory.)

The stellar angular momentum $j_\star(r < R_{\rm vir})$ jumps when satellite galaxies fall in, with the extent of the jump depending on both the trajectory of the orbit and its alignment relative to the existing stars. This is particularly striking for haloes A and C. In these two cases, the timing of the infall changes substantially as we modify the initial angular momentum: increased (resp. decreased) angular momentum modifications delay (resp. hasten) the infall time by as much as 500 Myr. In the case of halo C, the ×1.5 case has been excluded because the infall time is so delayed that it does not occur by the end of the simulation, as we previously noted.

The case of halo B is more complicated, with satellite galaxies entering the virial radius until the end of the simulation at $z = 2$. In this case, the angular momentum modification also changes the order in which mergers take place. As we previously commented, this complexity leads to our sole example of an angular momentum modification that has an unexpected effect; the dark blue line represents the ×0.66 case, which should end with the lowest angular

Downloaded from https://academic.oup.com/mnras/article/517/3/3459/6750247 by Deutsches Elektronen Synchrotron user on 08 December 2022

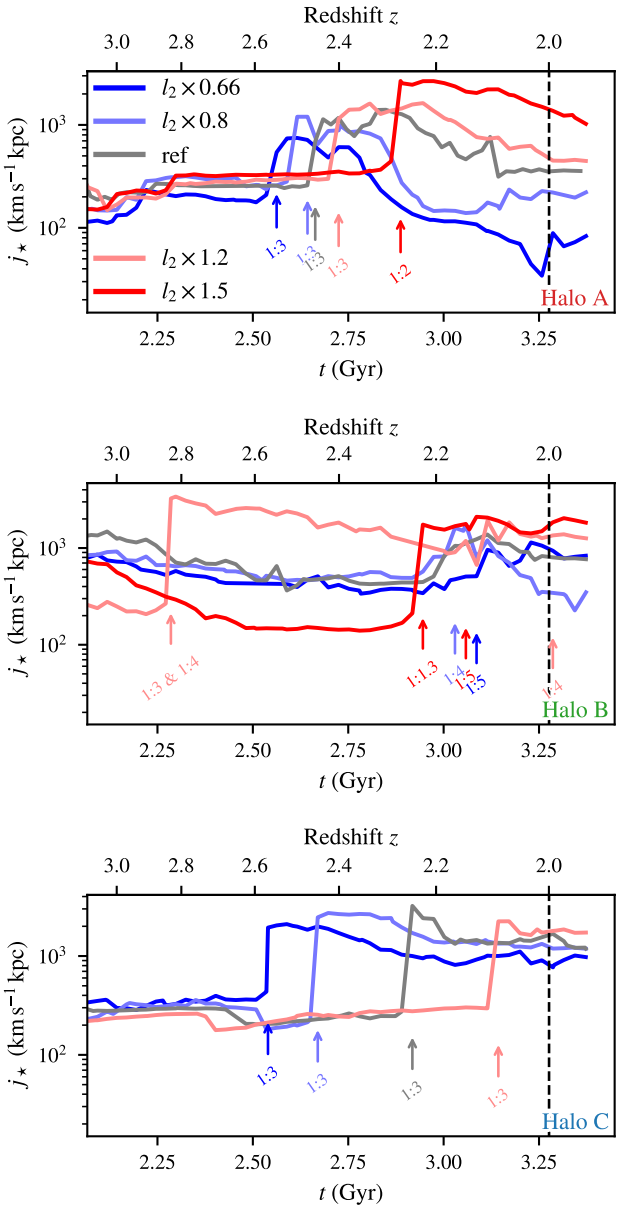

Figure 3. Evolution of the stellar angular momentum within the virial radius of haloes A, B, and C from top to bottom. We genetically modify the angular momentum in the initial conditions ($z = 200$) of the region that contains all baryons that will comprise the galaxy at $z = 2$. The initial angular momentum of the baryons is changed by factors of 0.66, 0.8, 1.2, and 1.5 (in dark blue, blue, red, and dark red, respectively) compared to a reference simulation (in grey). We show the time at which satellite galaxies cross the virial radius inwards as coloured arrows together with their stellar mass ratio compared to the central galaxy. This increase (resp. decrease) of the *initial* baryon angular momentum causes the specific angular momentum of the stars to increase (resp. decrease) by $z = 2$. It also changes the infall time of satellites in a systematic way, due to changes in their orbital angular momentum.

momentum but instead finishes with comparable angular momentum to the reference case. The complexity of the merger history precludes a full understanding, but we note that torques between satellites on either side of the halo boundary may have a role to play. Further investigation will require a larger sample of modified simulations.

In order to assess whether the DM halo spin correlates with the galactic spin, we measure the DM, baryons, and stellar angular momenta. If indeed the galaxy spin is inherited by the DM spin, we expect each galaxy to follow constant retention factor tracks $f_j = j/j_{\rm DM}$. We show the results in Fig. 4. Each of our tracks is a single object with constant stellar mass and DM mass within the virial radius. This allows us to start to understand the additional factors at play that drive the scatter in the $j_{\rm DM}$–$j_\star$ and $j_{\rm DM}$–$j_{\rm b}$ at the population level. In the case of a galaxy with no major satellite at $z = 2$ (halo A, in red), an increase of DM angular momentum correlates particularly tightly with an increase of stellar angular momentum. The correlation is 'superlinear', with an increasing fraction of angular momentum in stars as the DM angular momentum increases. At a population level, this would show up only as scatter in the relationship. In haloes with a more complex recent formation history and massive satellites (B and C), the relation between stellar and DM angular momenta becomes harder to predict. This suggests that, in the population as a whole, choosing relaxed haloes with no massive satellites may select systems with a particularly tight relationship between DM spin and galactic angular momentum.

The baryon angular momentum (right-hand panel of Fig. 4) comes much closer to tracking the DM angular momentum linearly, with a constant retention fraction for each family of galaxies. This suggests that a significant confounding factor in relating stellar and DM angular momenta is variations in the star formation efficiencies. Orbital angular momentum likely has little direct effect on star formation in a satellite, whereas high angular momentum within a central galaxy plausibly causes the disc to be more diffuse and therefore star formation rates to drop. Thus, the merger history can have effects on the stellar angular momentum, which do not show up in the total baryonic angular momentum. Our results suggest that, at the population level, the baryon-versus-DM angular momentum relation should therefore be tighter than the stellar-versus-DM angular momentum. Scatter in the population baryon-versus-DM angular momentum relation would primarily be caused by the different retention fractions, and such variations may themselves be predictable (e.g. from environmental considerations).

In summary, our results show (i) that angular momentum of stars in a given halo can be causally linked to the angular momentum of relevant patches of the initial conditions; (ii) the angular momentum of the central galaxy also follows the expected trend, provided that there are no unmerged massive satellites; and (iii) that the morphology of the central galaxy in the latter case changes significantly when the angular momentum is systematically altered. Finally, we show (iv) that, for galaxies simulated with different angular momenta but otherwise in minimally altered environments, there appears to be a tight link between the baryon and DM angular momenta. This correlation remains (albeit slightly weakened) when we compare stellar and DM angular momentum.

4 DISCUSSION AND CONCLUSIONS

In this paper, we tested for the first time whether the angular momentum of galaxies is predictably related to their initial conditions in the early universe. We employed zoom-in numerical simulations with state-of-the-art physics to study the formation of three simulated galaxies. We combined the angular momentum genetic modification technique (Cadiou et al. 2021) with Lagrangian tracer particles (Cadiou et al. 2019) to reconstruct the Lagrangian region from which all baryons in a galaxy originate, which we then genetically modified to either increase or decrease the angular momentum they will acquire through torques with the cosmological environment. Having resimulated using the modified initial conditions, we measured the

Downloaded from https://academic.oup.com/mnras/article/517/3/3459/6750247 by Deutsches Elektronen Synchrotron user on 08 December 2022

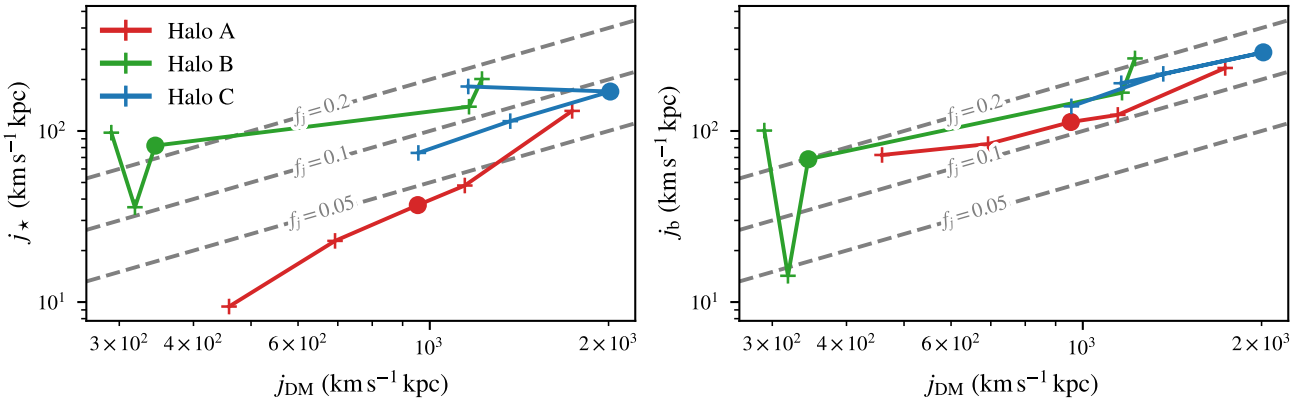

Figure 4. The DM specific angular momentum compared to the stellar (left-hand panel) and baryonic (right-hand panel) specific angular momentum within R_{vir} at $z = 2$. We indicate constant retention fraction $f_j = j/j_{DM}$ tracks with dashed lines. We find that DM and stellar specific angular momenta (left-hand panel) correlate, creating a 'track' for each individual galaxy. The correlation is tighter for our relaxed galaxy (halo A) and weaker in galaxies undergoing major merger (haloes B and C). The DM and baryonic specific angular momenta (right-hand panel) correlate more tightly, and follow tracks of near-constant retention factor. Deviations from the tracks appear in halo B, possibly as a result of a complex merger history at $z = 2$. The relative simplicity of the relation between DM and baryonic (as opposed to stellar) angular momentum suggests that star formation efficiencies vary due to changes in the merger history.

$z = 2$ angular momentum within the virial radius of the halo and in the galaxy itself.

In this initial study, we chose to focus on three galaxies with masses $M_\star \approx 10^{11}$ M$_\odot$ at $z = 2$; at this epoch, such galaxies exhibit a range of morphologies in observations. We successfully controlled the angular momentum of the stars inside their virial radius in the evolved universe (Fig. 1). We conclude that the angular momentum of stars in the virial radius of individual galaxies can thus be controlled from the initial conditions, and that gravitational torques with the large-scale structure do play a significant role in determining the value of the final angular momentum.[3] Our galaxy formation recipe includes state-of-the-art feedback prescriptions; thus, we have established that, despite the importance of self-regulation (Übler et al. 2014), galaxies at our chosen mass and redshift retain memory of the angular momentum in their cosmological initial conditions.

In the case of a relaxed galaxy with no large satellites at $z = 2$ (halo A), we were further able to control the central galaxy's angular momentum (Fig. 2). An increase of stellar angular momentum, $j_\star$, allows the formation of a more prominent and spatially extended disc. As stellar angular momentum increases, the v/σ parameter also increases, while the bulge fraction B/T decreases. These trends are in agreement with observations at $z \approx 1.5$, which show an anticorrelation between the stellar angular momentum and bulge fraction at fixed stellar mass (Gillman et al. 2020) and a correlation with v/σ parameter (Harrison et al. 2017). For this galaxy, we also show that the prominence of the disc is regulated by its angular momentum content, in agreement with the fact that, at fixed stellar mass, spiral galaxies are more angular momentum rich than elliptical ones (Fall 1983).

Our work establishes a clear demonstration of cause and effect: the early universe controls the stellar angular momentum in a galaxy, which, in turn, changes the morphology as parametrized by B/T and v/σ. In the future, we hope to increase the sample size to different stellar masses and observation redshifts to confirm that angular momentum is the key parameter driving scaling relations between $M_\star$, $j_\star$, B/T, v/σ, galaxy size, and galaxy morphology.

[3]Recall from Section 2.2 that genetic modifications of the initial angular momentum are achieved through scaling of the initial gravitational torques.

By studying the stellar angular momentum time evolution, we showed in Fig. 3 that, as satellites infall into the virial radius, the stellar angular momentum undergoes significant changes. As a result, stellar angular momentum is sensitive to the infall of major satellites, the timing of which changes substantially as we modify the initial angular momentum. Our results support the idea that angular momentum jumps with mergers (Vitvitska et al. 2002; Benson & Bower 2010; Benson et al. 2020), but additionally show that the angular momentum in the initial conditions determines the impact parameter and timing of mergers in a deterministic way. This dependence of the merger history on initial angular momentum could be used to investigate how impact parameter and timing determine the effects of a merger (e.g. Davies, Pontzen & Crain 2022).

During more complex periods of multiple mergers (as in the case of halo B), the interpretation of the origin of the stellar angular momentum is more ambiguous. Yet even in this case, we found that we can control the stellar angular momentum within the virial radius except when we tried to increase it by too large a factor ($\times 1.5$ in the initial conditions). This ability to reliably control angular momentum under challenging circumstances opens up the possibility of future simulations gaining insight into the internal physical processes of galaxy formation, for example by testing whether decreasing a galaxy's angular momentum drives the growth rate of the central supermassive black hole (as suggested in Bellovary et al. 2013; Curtis & Sijacki 2016; Anglés-Alcázar et al. 2017).

Our results support the idea that the DM angular momentum and the galactic angular momentum are linked. This is in agreement with statistical studies that found that, at fixed stellar mass, DM haloes with larger spins host faster-rotating galaxies (Kimm et al. 2011; Genel et al. 2015; Teklu et al. 2015; Rodriguez-Gomez et al. 2022), albeit with significant scatter. By comparing the DM, stellar, and baryon angular momenta in galaxies with controlled changes to their formation history, we can go one step further and start investigating the origin of the scatter observed in the j_{DM}–$j_\star$ relation at the population level. We showed that the relation between j_{DM} and j_b in our galaxies is almost linear, suggesting that a major source of scatter in the j_{DM}–$j_\star$ relation is the impact of the angular momentum on local star formation efficiency. Our results also suggest that relaxed haloes with no massive satellites will exhibit a particularly tight relationship between DM spin and galactic angular momentum.

Downloaded from https://academic.oup.com/mnras/article/517/3/3459/6750247 by Deutsches Elektronen Synchrotron user on 08 December 2022

Our results also suggest that predicting stellar angular momentum and hence disc alignments *ab initio* may be possible. We have shown that, once the patch of the initial conditions from which the baryons accrete is identified, the final stellar angular momentum closely tracks the patch's initial spin. Because the stars occupy the deepest part of the potential, their corresponding patch is likely to be predictable using approximate or machine learning methods (Lucie-Smith et al. 2018; Lucie-Smith, Peiris & Pontzen 2019). Current predictions based instead on the DM patch (Porciani, Dekel & Hoffman 2002; Park et al. 2022, fig. 19) suffer from particles in the outskirts dominating the angular momentum budget (Cadiou et al. 2021). Focusing on baryonic patches could enable more precise predictions of the intrinsic alignment signal (see Kiessling et al. 2015, for a review), lessening uncertainty in a key systematic for forthcoming weak-lensing surveys.

ACKNOWLEDGEMENTS

CC thanks C. Pichon, Y. Dubois, and J. Devriendt, who provided useful feedback on the project. We thank M. Fall and the referee for their stimulating comments that contributed to improving the paper. This project has received funding from the European Union's Horizon 2020 research and innovation programme under grant agreement no. 818085 GMGalaxies. This work used computing equipment funded by DiRAC (10 Mcpu hr, project dp160). Data analysis was carried out on facilities supported by the Research Capital Investment Fund (RCIF) provided by UKRI and partially funded by the UCL Cosmoparticle Initiative. Part of the project made use of the Infinity Cluster hosted by Institut d'Astrophysique de Paris. The work of HVP was partially supported by the Göran Gustafsson Foundation for Research in Natural Sciences and Medicine and the European Research Council (ERC) under the European Union's Horizon 2020 research and innovation programme (grant agreement no. 101018897 CosmicExplorer). This work has been enabled by support from the research project grant 'Understanding the Dynamic Universe' funded by the Knut and Alice Wallenberg Foundation under Dnr KAW 2018.0067. AP was supported by the Royal Society. The analysis was carried out using COLOSSUS (Diemer 2018), JUPYTER notebooks (Kluyver et al. 2016), GENETIC 1.3.5 (Pontzen et al. 2022), MATPLOTLIB (Hunter 2007), NUMPY (Harris et al. 2020), PYNBODY (Pontzen et al. 2013), PYTHON, TANGOS (Pontzen & Tremmel 2018), and YT (Turk et al. 2011).

AUTHOR CONTRIBUTIONS

The main roles of the authors were, using the CRediT (Contribution Roles Taxonomy) system (https://authorservices.wiley.com/author-resources/Journal-Authors/open-access/credit.html), as follows:

CC: conceptualization, methodology, validation, investigation, data curation, formal analysis, writing – original draft, and visualization.

AP: conceptualization, methodology, funding acquisition, writing – review and editing, and validation.

HVP: conceptualization, writing – review and editing, and validation.

DATA AVAILABILITY

The data underlying this paper will be shared on reasonable request to the corresponding author.

REFERENCES

Anglés-Alcázar D., Davé R., Faucher-Giguère C.-A., Özel F., Hopkins P. F., 2017, MNRAS, 464, 2840
Athanassoula E., Rodionov S. A., Peschken N., Lambert J. C., 2016, ApJ, 821, 90
Aubert D., Pichon C., Colombi S., 2004, MNRAS, 352, 376
Aung H., Mandelker N., Nagai D., Dekel A., Birnboim Y., 2019, MNRAS, 490, 181
Barnes J. E., Hernquist L., 1996, ApJ, 471, 115
Bellovary J., Brooks A., Volonteri M., Governato F., Quinn T., Wadsley J., 2013, ApJ, 779, 136
Benson A. J., 2012, New Astron., 17, 175
Benson A. J., Bower R., 2010, MNRAS, 405, 1573
Benson A., Behrens C., Lu Y., 2020, MNRAS, 496, 3371
Brook C. B. et al., 2011, MNRAS, 415, 1051
Bullock J. S., Dekel A., Kolatt T. S., Kravtsov A. V., Klypin A. A., Porciani C., Primack J. R., 2001, ApJ, 555, 240
Cadiou C., Dubois Y., Pichon C., 2019, A&A, 621, A96
Cadiou C., Pontzen A., Peiris H. V., 2021, MNRAS, 502, 5480
Cadiou C., Dubois Y., Pichon C., 2022, MNRAS, 514, 5429
Chisari N. E. et al., 2017, MNRAS, 472, 1163
Cornuault N., Lehnert M. D., Boulanger F., Guillard P., 2018, A&A, 610, A75
Cox T. J., Dutta S. N., Di Matteo T., Hernquist L., Hopkins P. F., Robertson B., Springel V., 2006, ApJ, 650, 791
Curtis M., Sijacki D., 2016, MNRAS, 463, 63
Danovich M., Dekel A., Hahn O., Ceverino D., Primack J., 2015, MNRAS, 449, 2087
Davies J. J., Pontzen A., Crain R. A., 2022, MNRAS, 515, 1430
Dekel A., Birnboim Y., 2006, MNRAS, 368, 2
Dekel A., Burkert A., 2014, MNRAS, 438, 1870
Diemer B., 2018, ApJS, 239, 35
Doroshkevich A. G., 1970, Astrofizika, 6, 581
Dubois Y., Pichon C., Haehnelt M., Kimm T., Slyz A., Devriendt J., Pogosyan D., 2012, MNRAS, 423, 3616
Dubois Y., Pichon C., Devriendt J., Silk J., Haehnelt M., Kimm T., Slyz A., 2013, MNRAS, 428, 2885
Dubois Y., Volonteri M., Silk J., Devriendt J., Slyz A., 2014, MNRAS, 440, 2333
Dubois Y. et al., 2021, A&A, 651, A109
Espejo Salcedo J. M., Glazebrook K., Fisher D. B., Sweet S. M., Obreschkow D., Swinbank A. M., Gillman S., Tiley A. L., 2022, MNRAS, 509, 2318
Fall S. M., 1983, in Athanassoula E., ed., Proc. IAU Symp. 100, Internal Kinematics and Dynamics of Galaxies. Reidel, Dordrecht, p. 391
Fall S. M., Efstathiou G., 1980, MNRAS, 193, 189
Fall S. M., Romanowsky A. J., 2018, ApJ, 868, 133
Garrison-Kimmel S. et al., 2018, MNRAS, 481, 4133
Geen S., Rosdahl J., Blaizot J., Devriendt J., Slyz A., 2015, MNRAS, 448, 3248
Genel S., Fall S. M., Hernquist L., Vogelsberger M., Snyder G. F., Rodriguez-Gomez V., Sijacki D., Springel V., 2015, ApJ, 804, L40
Gillman S. et al., 2020, MNRAS, 492, 1492
Governato F. et al., 2009, MNRAS, 398, 312
Guillet T., Teyssier R., 2011, J. Comput. Phys., 230, 4756
Guo Q. et al., 2011, MNRAS, 413, 101
Haardt F., Madau P., 1996, ApJ, 461, 20
Harris C. R. et al., 2020, Nature, 585, 357
Harrison C. M. et al., 2017, MNRAS, 467, 1965
Hopkins P. F., Cox T. J., Younger J. D., Hernquist L., 2009, ApJ, 691, 1168
Hunter J. D., 2007, Comput. Sci. Eng., 9, 90
Ivezić Ž. et al., 2019, ApJ, 873, 111
Jackson R. A., Martin G., Kaviraj S., Laigle C., Devriendt J. E. G., Dubois Y., Pichon C., 2020, MNRAS, 494, 5568
Jiang F. et al., 2019, MNRAS, 488, 4801
Kiessling A. et al., 2015, Space Sci. Rev., 193, 67
Kimm T., Devriendt J., Slyz A., Pichon C., Kassin S. A., Dubois Y., 2011, preprint (arXiv:1106.0538)

Downloaded from https://academic.oup.com/mnras/article/517/3/3459/6750247 by Deutsches Elektronen Synchrotron user on 08 December 2022

Kimm T., Cen R., Devriendt J., Dubois Y., Slyz A., 2015, MNRAS, 451, 2900
Kluyver T. et al., 2016, in Loizides F., Scmidt B., eds, 20th International Conference on Electronic Publishing. IOS Press, Amsterdam, The Netherlands, p. 87
Kroupa P., 2001, MNRAS, 322, 231
Lagos C. D. P. et al., 2018, MNRAS, 473, 4956
Laureijs R. et al., 2011, preprint (arXiv:1110.3193)
Li J., Obreschkow D., Power C., Lagos C. d. P., 2022, MNRAS, 515, 437
Liao S., Gao L., Frenk C. S., Guo Q., Wang J., 2017, MNRAS, 470, 2262
Lotz J. M., Jonsson P., Cox T. J., Primack J. R., 2008, MNRAS, 391, 1137
Lucie-Smith L., Peiris H. V., Pontzen A., Lochner M., 2018, MNRAS, 479, 3405
Lucie-Smith L., Peiris H. V., Pontzen A., 2019, MNRAS, 490, 331
McKinney J. C., Tchekhovskoy A., Blandford R. D., 2012, MNRAS, 423, 3083
Mandelker N., Padnos D., Dekel A., Birnboim Y., Burkert A., Krumholz M. R., Steinberg E., 2016, MNRAS, 463, 3921
Mandelker N., Nagai D., Aung H., Dekel A., Padnos D., Birnboim Y., 2019, MNRAS, 484, 1100
Mandelker N., Nagai D., Aung H., Dekel A., Birnboim Y., van den Bosch F. C., 2020, MNRAS, 494, 2641
Martin G., Kaviraj S., Devriendt J. E. G., Dubois Y., Pichon C., 2018, MNRAS, 480, 2266
Mo H. J., Mao S., White S. D. M., 1998, MNRAS, 295, 319
Naab T., Burkert A., 2003, ApJ, 597, 893
Nuñez-Castiñeyra A., Nezri E., Devriendt J., Teyssier R., 2021, MNRAS, 501, 62
Padnos D., Mandelker N., Birnboim Y., Dekel A., Krumholz M. R., Steinberg E., 2018, MNRAS, 477, 3293
Park M.-J. et al., 2019, ApJ, 883, 25
Park M.-J. et al., 2021, ApJS, 254, 2
Park C. et al., 2022, ApJ, 937, 15
Peebles P. J. E., 1969, ApJ, 155, 393
Pichon C., Pogosyan D., Kimm T., Slyz A., Devriendt J., Dubois Y., 2011, MNRAS, 418, 2493
Planck Collaboration XXIII, 2015, A&A, 594, A13
Pontzen A., Tremmel M., 2018, ApJS, 237, 23
Pontzen A., Roškar R., Stinson G., Woods R., 2013, Astrophysics Source Code Library, record ascl:1305.002
Pontzen A., Cadiou C., Stopyra S., Roth N., Rey M. P., 2022, Pynbody/genetIC: Version 1.3.5, Zenodo, doi:10.5281/zenodo.6327377
Porciani C., Dekel A., Hoffman Y., 2002, MNRAS, 332, 339
Power C., Navarro J. F., Jenkins A., Frenk C. S., White S. D. M., Springel V., Stadel J., Quinn T., 2003, MNRAS, 338, 14
Ramsøy M., Slyz A., Devriendt J., Laigle C., Dubois Y., 2021, MNRAS, 502, 351
Robertson B., Bullock J. S., Cox T. J., Di Matteo T., Hernquist L., Springel V., Yoshida N., 2006, ApJ, 645, 986
Rodriguez-Gomez V. et al., 2022, MNRAS, 512, 5978
Romanowsky A. J., Fall S. M., 2012, ApJS, 203, 17
Rosen A., Bregman J. N., 1995, ApJ, 440, 634
Roth N., Pontzen A., Peiris H. V., 2016, MNRAS, 455, 974
Shakura N. I., Sunyaev R. A., 1973, A&A, 24, 337
Somerville R. S., Hopkins P. F., Cox T. J., Robertson B. E., Hernquist L., 2008, MNRAS, 391, 481
Stewart K. R., Kaufmann T., Bullock J. S., Barton E. J., Maller A. H., Diemand J., Wadsley J., 2011, ApJ, 735, L1
Stewart K. R. et al., 2017, ApJ, 843, 47
Stopyra S., Pontzen A., Peiris H., Roth N., Rey M. P., 2021, ApJS, 252, 28
Sutherland R. S., Dopita M. A., 1993, ApJS, 88, 253
Tamburri S., Saracco P., Longhetti M., Gargiulo A., Lonoce I., Ciocca F., 2014, A&A, 570, A102
Teklu A. F., Remus R.-S., Dolag K., Beck A. M., Burkert A., Schmidt A. S., Schulze F., Steinborn L. K., 2015, ApJ, 812, 29
Tenneti A., Mandelbaum R., Di Matteo T., Feng Y., Khandai N., 2014, MNRAS, 441, 470
Teyssier R., 2002, A&A, 385, 337
Tillson H., Devriendt J., Slyz A., Miller L., Pichon C., 2015, MNRAS, 449, 4363
Toro E. F., Spruce M., Speares W., 1994, Shock Waves, 4, 25
Trebitsch M. et al., 2021, A&A, 653, A154
Troxel M. A., Ishak M., 2015, Phys. Rep., 558, 1
Turk M. J., Smith B. D., Oishi J. S., Skory S., Skillman S. W., Abel T., Norman M. L., 2011, ApJS, 192, 9
Tweed D., Devriendt J., Blaizot J., Colombi S., Slyz A., 2009, A&A, 506, 647
Übler H., Naab T., Oser L., Aumer M., Sales L. V., White S. D. M., 2014, MNRAS, 443, 2092
van Leer B., 1979, J. Comput. Phys., 32, 101
Velliscig M. et al., 2015, MNRAS, 453, 721
Vitvitska M., Klypin A. A., Kravtsov A. V., Wechsler R. H., Primack J. R., Bullock J. S., 2002, ApJ, 581, 799
White S., 1984, ApJ, 286, 38
Zeng G., Wang L., Gao L., 2021, MNRAS, 507, 3301
Zolotov A. et al., 2015, MNRAS, 450, 2327

APPENDIX A: TECHNICAL DESCRIPTION OF THE SIMULATION SET-UP

The simulations are started with a coarse grid of 512^3 (level 7) and several nested grids with increasing levels of refinement up to level 12, corresponding to a DM mass resolution of, respectively, 8.2×10^8, 1×10^8, 1.3×10^7, and $1.6 \times 10^6\,\mathrm{M}_\odot$.

Particles (DM, stars, and black holes) are moved with a leapfrog scheme, and to compute their contribution to the gravitational potential, their mass is projected on to the mesh with a cloud-in-cell interpolation. Gravitational acceleration is obtained by computing the gravitational potential through the Poisson equation numerically obtained with a conjugate gradient solver on levels above 12, and a multigrid scheme (Guillet & Teyssier 2011) otherwise. We include hydrodynamics in the simulations, in which a system of non-linear conservation laws is solved with the MUSCL-Hancock scheme (van Leer 1979) using a linear reconstruction of the conservative variables at cell interfaces with the minmod total variation diminishing scheme, and with the use of the Harten-Lax-van Leer-Contact (HLLC) approximate Riemann solver (Toro, Spruce & Speares 1994) to predict the upstream Godunov flux. We allow the mesh to be refined according to a quasi-Lagrangian criterion: if $\rho_{\rm DM} + \rho_{\rm b}/f_{\rm b/DM} > 8m_{\rm DM,\,res}/\Delta x^3$, where $\rho_{\rm DM}$ and $\rho_{\rm b}$ are, respectively, the DM and baryon density [including stars, gas, and supermassive black holes (SMBHs)], and where $f_{\rm b/DM}$ is the universal baryon-to-DM mass ratio. Conversely, an oct (8 cells) is de-refined when this local criterion is not fulfilled. The maximum level of refinement is also enforced up to 4 minimum cell size distance around all SMBHs. The simulations have a roughly constant proper resolution of 35 pc (one additional maximum level of refinement at expansion factors 0.1 and 0.2 corresponding to a maximum level of refinement of, respectively, 19 and 20), a star particle mass resolution of $m_{\star,\rm res} = 1.1 \times 10^4\,\mathrm{M}_\odot$, and a gas mass resolution of $2.2 \times 10^5\,\mathrm{M}_\odot$ in the refined region. Each Monte Carlo tracer samples a mass of $m_{\rm t} = 3.9 \times 10^4\,\mathrm{M}_\odot$ ($N_{\rm tot} \approx 1.1 \times 10^7$ particles). There is on average 0.3 tracer per star and 22 per initial gas resolution element. Cells of size 35 pc and gas density of $40\,\mathrm{cm}^{-3}$ contain on average one tracer per cell.

The simulations include a metal-dependent tabulated gas cooling function following Sutherland & Dopita (1993) for gas with temperature above $T > 10 \times 10^4\,\mathrm{K}$. The metallicity of the gas in the simulation is initialized to $Z_0 = 10^{-3}\,\mathrm{Z}_\odot$ to allow further cooling below 10^4 K down to $T_{\rm min} = 10\,\mathrm{K}$ (Rosen & Bregman 1995). Reionization occurs at $z = 8.5$ using the Haardt & Madau (1996) UV background model and assuming gas self-shielding above

Downloaded from https://academic.oup.com/mnras/article/517/3/3459/6750247 by Deutsches Elektronen Synchrotron user on 08 December 2022

$10^{-2}\,\mathrm{cm}^{-3}$. Star formation is allowed above a gas number density of $n_0 = 10\,\mathrm{cm}^{-3}$ with a Schmidt law, and with an efficiency ϵ_{ff} that depends on the gravo-turbulent properties of the gas (for a comparison with a constant efficiency, see Nuñez-Castiñeyra et al. 2021). The stellar population is sampled with a Kroupa (2001) initial mass function. The mass-loss fraction from supernova explosions is $\eta_{\mathrm{SN}} = 32$ per cent with a metal yield (mass ratio of the newly formed metals over the total ejecta) of 0.05. Type II supernovae are modelled with the mechanical feedback model of Kimm et al. (2015) with a boost in momentum due to early UV pre-heating of the gas following Geen et al. (2015). The simulations also track the formation of SMBHs and their energy release through AGN feedback. SMBH accretion assumes an Eddington-limited Bondi–Hoyle–Lyttleton accretion rate in jet mode (radio mode) and thermal mode (quasar mode) using the model of Dubois et al. (2012). The jet is modelled self-consistently by following the angular momentum of the accreted material and the spin of the black hole (Dubois et al. 2014). The radiative efficiency and spin-up rate of the SMBH are computed assuming the radiatively efficient thin accretion disc from Shakura & Sunyaev (1973) for the quasar mode, while the feedback efficiency and spin-up rate in the radio mode follow the prediction of the magnetically choked accretion flow model for accretion discs from McKinney, Tchekhovskoy & Blandford (2012). SMBHs are created with a seed mass of $10^5\,\mathrm{M}_\odot$. For the exact details of the spin-dependent SMBH accretion and AGN feedback, see Dubois et al. (2021).

This paper has been typeset from a TEX/LATEX file prepared by the author.

Downloaded from https://academic.oup.com/mnras/article/517/3/3459/6750247 by Deutsches Elektronen Synchrotron user on 08 December 2022